Rare Metal Materials and Engineering
Volume 54, Issue 4, April 2025
Available online at www.rmme.ac.cn

Science Press

Cite this article as: Zhang Jun, Liu Xi, Li Yi, et al. Introducing High-Volume-Fraction Ultrafine Grains to Obtain Superior Balance of Strength and Electrical Conductivity for Cu/Al_2O_3 Composite[J]. Rare Metal Materials and Engineering, 2025, 54(04): 908-919. DOI: https://doi.org/10.12442/j.issn.1002-185X.20240107.

ARTICLE

Introducing High-Volume-Fraction Ultrafine Grains to Obtain Superior Balance of Strength and Electrical Conductivity for Cu/Al_2O_3 Composite

Zhang Jun[1,2], Liu Xi[2,3], Li Yi[2,3], Chang Guo[2,4], Peng Haoran[2,4], Zhang Shuang[2,4], Huang Qi[1], Zhao Xueni[1], Li Liang[2,4], Huo Wangtu[2,4]

[1] College of Mechanical and Electrical Engineering, Shaanxi University of Science and Technology, Xi'an 710021, China; [2] Advanced Materials Research Central, Northwest Institute for Nonferrous Metal Research, Xi'an 710016, China; [3] School of Materials Science and Engineering, Xi'an University of Technology, Xi'an 710048, China; [4] State Key Laboratory of Porous Metal Materials, Northwest Institute for Nonferrous Metal Research, Xi'an 710016, China

Abstract: Compared with Cu/Al_2O_3 composites, high-strength Cu/Al_2O_3 composites usually exhibit obviously deteriorated electrical conductivity. A chemical and mechanical alloying-based strategy was adopted to fabricate ultrafine composite powders with low-content reinforcement and constructed a combined structure of Cu ultrafine powders covered with in-situ Al_2O_3 nanoparticles. After consolidation at a relatively lower sintering temperature of 550 ℃, high-volume-fraction ultrafine grains were introduced into the Cu/Al_2O_3 composite, and many in-situ Al_2O_3 nanoparticles with an average size of 11.7±7.5 nm were dispersed homogeneously in the Cu grain. Results show that the composite demonstrates an excellent balance of high tensile strength (654±1 MPa) and high electrical conductivity (84.5±0.1% IACS), which is ascribed to the synergistic strengthening effect of ultrafine grains, dislocations, and in-situ Al_2O_3 nanoparticles. This approach, which utilizes ultrafine composite powder with low-content reinforcement as a precursor and employs low-temperature and high-pressure sintering subsequently, may hold promising potential for large-scale industrial production of high-performance oxide dispersion strengthened alloys.

Key words: Cu/Al_2O_3 composite; ultrafine grain; in-situ Al_2O_3 nanoparticle; strengthening mechanism; electrical conductivity

1 Introduction

Cu/Al_2O_3 composites are widely used in modern industry, such as integrated circuit lead frames, electric vacuum devices, heat exchangers, and electrical contact materials, owing to their excellent mechanical, electrical and thermal properties[1]. It is well recognized that materials with high strength and high electrical conductivity are crucial for ensuring service safety and minimizing energy loss, making them a primary focus for researchers[2–3]. While increasing the quantity of second-phase nanoparticles can enhance the strength of composites, it often results in nanoparticle agglomeration and a reduction in electrical conductivity[4–5]. More importantly, the dispersion strengthening effect in Cu/Al_2O_3 composites is reaching its limit. Compared with second-phase nanoparticles, ultrafine Cu grains (less than 1 μm) possess both high strength and high conductivity, without altering chemical composition[6–7]. The respective advantages of reinforcement and ultrafine grains can be integrated properly to achieve synergistic strengthening effects on the

Received date: April 29, 2024
Foundation item: Foundation of Northwest Institute for Non-ferrous Metal Research (YK2020-9, ZZXJ2203); Capital Projects of Financial Department of Shaanxi Province (YK22C-12); National Natural Science Foundation of China (62204207); Innovation Capability Support Plan in Shaanxi Province of China (2022KJXX-82, 2023KJXX-083); Natural Science Foundation of Shaanxi Province (2022JQ-332); Shaanxi Innovative Research Team for Key Science and Technology (2023-CX-TD-46); Key Research and Development Projects of Shaanxi Province (2024GX-YBXM-351)
Corresponding author: Zhao Xueni, Ph. D., Professor, College of Mechanical and Electrical Engineering, Shaanxi University of Science and Technology, Xi'an 710021, P. R. China, E-mail: zhaoxueni@sust.edu.cn; Li Liang, Ph. D., Advanced Materials Research Central, Northwest Institute for Nonferrous Metal Research, Xi'an 710016, P. R. China, E-mail: fid1991@163.com; Huo Wangtu, Ph. D., Professor, Advanced Materials Research Central, Northwest Institute for Nonferrous Metal Research, Xi'an 710016, P. R. China, E-mail: huowt@c-nin.com

basis of different physical properties; thus, introducing high-volume-fraction ultrafine grains into metal matrix composites is one of the most promising strategies to further improve the overall performance[8–11].

Great efforts have been devoted to develop metal matrix composites with ultrafine grains by powder processing and thermomechanical powder consolidation[9,12]. Powder processing can be classified into two typical strategies. The first strategy involves the fabrication of metallic nano or ultrafine powders mixed with second-phase nanoparticles by thermochemical process[13–16]. The precursor powder is produced by drying the mixed salt solutions containing matrix and reinforcement elements and then reduced to form ultrafine composite powder. Due to the molecular-level mixing of salt solutions, this method enables nano-level dispersion of second-phase nanoparticles in the metal matrix. As a result, the resulting composites possess ultrafine grain structures and excellent mechanical properties, as demonstrated in Cu/Y_2O_3 composite[14], Mo/La_2O_3 composite[16], and W/HfO_2 composite[17]. For instance, the Mo/La_2O_3 composite with ultrafine powder fabricated by the liquid-liquid doping method achieves the formation of ultrafine grains with a size of 500 nm, significantly enhancing the tensile strength from 534 MPa to 865 MPa. However, the productivity of composites through these methods is severely restricted by the solubility of inorganic salts in water. The second strategy employs mechanical alloying to fabricate nanocrystalline or ultrafine-grained metal powder mixed with second-phase nanoparticles[18–20]. During this process, the metal powders repeatedly undergo severe plastic deformation, cold welding, and fracture, and the second-phase nanoparticles are trapped in the metal grain interior, resulting in the formation of nanocrystals and a dispersed distribution of second-phase nanoparticles[9, 21–22]. This mature method can mix the powders uniformly and easily control the composition of the composite. For instance, Zhou et al[21] fabricated a Cu/Al_2O_3 composite with an average grain size of 552 nm by high-energy ball milling, and obtained a high tensile strength of 650 MPa and an electrical conductivity of 71.1% IACS (international annealing copper standard). However, contaminations will inevitably be introduced into the composite powder during high-energy ball milling[23], leading to the deterioration of electrical conductivity and poor interfacial bonding strength between the metal matrix and reinforcement.

Moreover, as the nanocrystalline or ultrafine-grained metal powder is sensitive to the sintering temperature, the powder consolidation process is critical. When the sintering temperature is much higher than the recrystallization temperature, the grain boundary migrates easily and obvious grain growth occurs. Therefore, researchers usually increase the quantity of reinforcement to prevent grain growth during high-temperature sintering processes[10, 21]. Recent studies have suggested that high pressure provides effective pathways to sinter nanocrystalline or ultrafine-grained metal powder at relatively low temperature, enabling the fabrication of highly dense pure or low-content nanoparticle-reinforced materials while suppressing grain growth[24–25]. For example, Li et al[22] produced 0.8vol% C-reinforced nanocomposites with a grain size of 63 nm by consolidating nanocrystalline composite powder at a pressure of 600 MPa and temperature of 300 ℃, and the nanocomposites exhibited a high density (>99%) and excellent comprehensive properties. Therefore, low-temperature and high-pressure sintering is a feasible method to fabricate highly dense low-content nanoparticle-reinforced materials with high-volume-fraction ultrafine grains to maintain high strength and high electrical conductivity.

Motivated by the above considerations, we developed a novel strategy based on chemical and mechanical alloying to fabricate low-content in-situ Al_2O_3 nanoparticles and high-volume-fraction ultrafine grains in Cu matrix composites to enhance the overall performance. The key to this approach relays in refining the Cu powder and constructing the combined structure of Cu ultrafine powders covered with in-situ Al_2O_3 nanoparticles, facilitating the low-temperature and high-pressure sintering of Cu/Al_2O_3 composites.

2 Experiment

Fig. 1 shows the fabrication schematic of Cu/Al_2O_3 composites. $Al(NO_3)_3·9H_2O$ was dissolved in ethanol with 0.2wt% Al in Cu/Al_2O_3 composites by sonication to obtain a salt solution. Subsequently, the electrolytic Cu powder was mixed with the salt solution by stirring, and then the mixture was dried at 60 ° C under vacuum. The obtained $Cu/Al(NO_3)_3$ precursor powders were ball milled in an Ar atmosphere at a rotation speed of 300 r/min, with an interruption of 10 min every 30 min for durations of 12, 24, and 36 h, marked as C-12 h, C-24

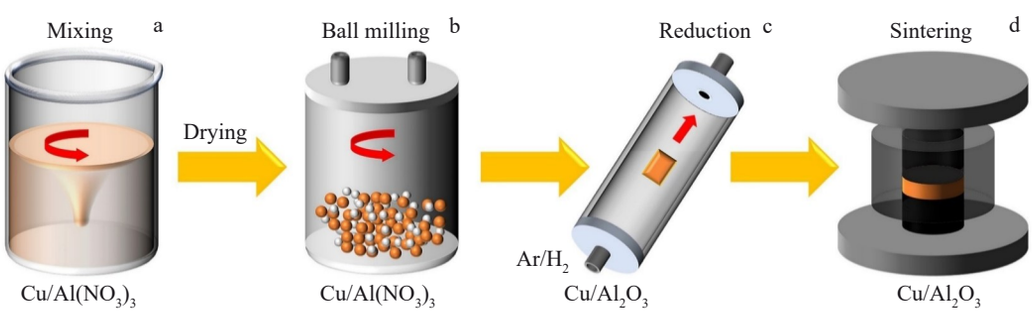

Fig.1 Fabrication schematics of Cu/Al_2O_3 composites: (a) mixing pure Cu powder and $Al(NO_3)_3$/ethanol solution; (b) milling $Cu/Al(NO_3)_3$ precursor powders; (c) reducing $Cu/Al(NO_3)_3$ precursor powders; (d) sintering Cu/Al_2O_3 powder

h, and C-36 h, respectively. The ball-to-powder mass ratio was 2.7: 1. Afterward, the thermal reduction of $Cu/Al(NO_3)_3$ precursor powders was conducted in a H_2/Ar atmosphere at 400 ℃ to form Cu/Al_2O_3 composite powders. Finally, the as-prepared Cu/Al_2O_3 composite powders were placed in a cylindrical mold with an inner diameter of 30 mm, and sintered at a uniaxial pressure of 400 MPa and temperature of 550 ℃ for 5 min under vacuum. As a reference, the fabrication of pure Cu (Cu-36 h) was carried out by the same processing route with a ball milling time of 36 h.

Inductively coupled plasma-atomic emission spectrometer (ICP-AES, iCAP 7000 SERIES) was used to determine the chemical composition of the powders. X-ray diffraction (XRD, Bruker D8 ADVANCE) observation was performed to analyze the microstrain and dislocation density of Cu-36 h and the composites. The Archimedes method was employed to test the density of the bulk materials. Scanning electron microscope (SEM, Zeiss GeminiSEM 500) and transmission electron microscope (TEM, FEI Talos F200X) together with energy dispersive spectroscopy (EDS) mapping were used to investigate the morphologies and microstructures of the powders and composites. Electron backscattered diffraction (EBSD, FEI Sicos) was employed to characterize the grain size distribution and kernel average misorientation (KAM). A universal tester (UTM5105X) and electrical conductivity gauge (D60K) were used to measure the mechanical and electrical properties of Cu-36 h and composites, respectively.

3 Results and Discussion

3.1 Powder microstructures

Table 1 lists the chemical composition of pure Cu powder and composite powders with different ball milling durations after thermal reduction. Few contaminants are introduced into the powders after high-energy ball milling, which do not significantly deteriorate the electrical conductivity of the composites. Fig. 2 and Fig. 3 show the morphologies of powders with different ball milling durations before and after thermal reduction, respectively. The original electrolytic Cu powders with particle sizes of 4 – 7 μm suffer from severe plastic deformation and become agglomerated after ball milling, while the composite powders are obviously refined. Correspondingly, in the XRD results (Fig.4), the full-width at half-maximum (FWHM) of the Cu phase of the composite powder is larger than that of pure Cu powder (Cu-36 h), indicating a smaller Cu crystallite (grain) size in the composite powder according to the well-known Scherrer formula[17]. Moreover, Cu ultrafine powders are obtained without significant agglomeration, which may be caused by the fact that the corrosion of the Cu powder surface by the $Al(NO_3)_3$ solution impedes cold welding during ball milling. After thermal reduction at 400 ℃ , the $Al(NO_3)_3$ salt is decomposed to form in-situ Al_2O_3 nanoparticles[13]. It is obvious that the Cu ultrafine powders are covered with a large number of in-situ Al_2O_3 nanoparticles, as shown in Fig.3f.

Table 1 Chemical composition of pure Cu powders and composite powders after thermal reduction (wt%)

Powder	Al	Fe	Cr	Ni	Cu
Original Cu powder	<0.010	<0.010	<0.010	<0.010	Bal.
Cu-36 h	<0.010	0.029	<0.010	<0.010	Bal.
C-12 h	0.180	<0.010	<0.010	<0.010	Bal.
C-24 h	0.180	0.012	<0.010	<0.010	Bal.
C-36 h	0.200	0.018	<0.010	<0.010	Bal.

3.2 Microstructures of composites

The relative density and microstructures of Cu-36 h and composites after low-temperature and high-pressure sintering are shown in Table 2 and Fig. 5, respectively. Highly dense composites are obtained, and many in-situ Al_2O_3 nanoparticles are observed in the composites (Fig. $5b_2$ – $5d_2$), corresponding to the powder characteristics. With increasing the ball milling durations, the overall distribution of in-situ Al_2O_3 nanoparticles becomes more homogeneous in the composites. Fig.6 displays typical EBSD images and grain size distributions of Cu-36 h and composites. The average grain sizes of Cu-36 h and C-36 h are both smaller than 1 μm, reaching 729±570 and

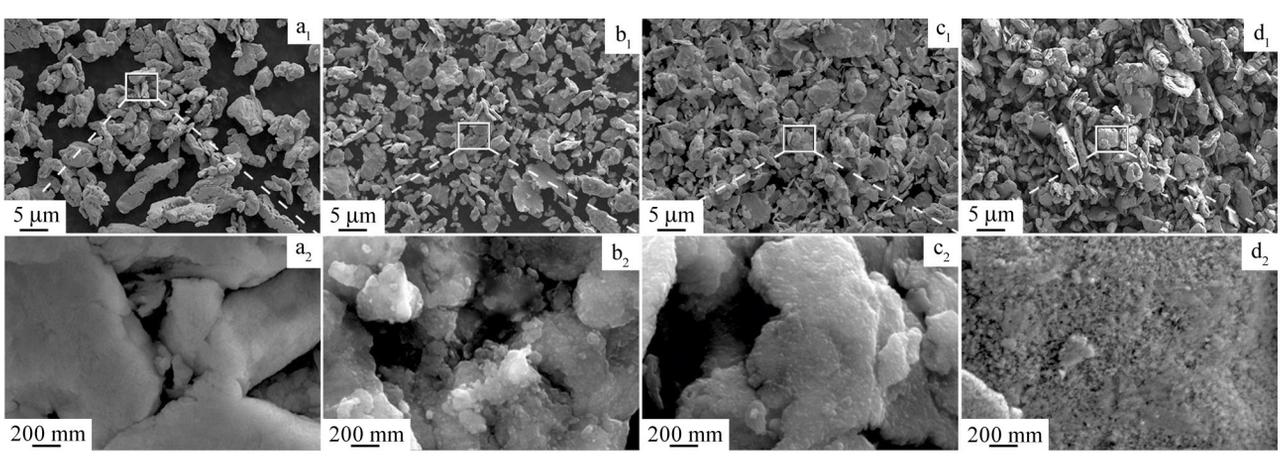

Fig.2 Morphologies of pure Cu powders and composite powders before thermal reduction: (a_1–a_2) Cu-36 h, (b_1–b_2) C-12 h, (c_1–c_2) C-24 h, and (d_1–d_2) C-36 h

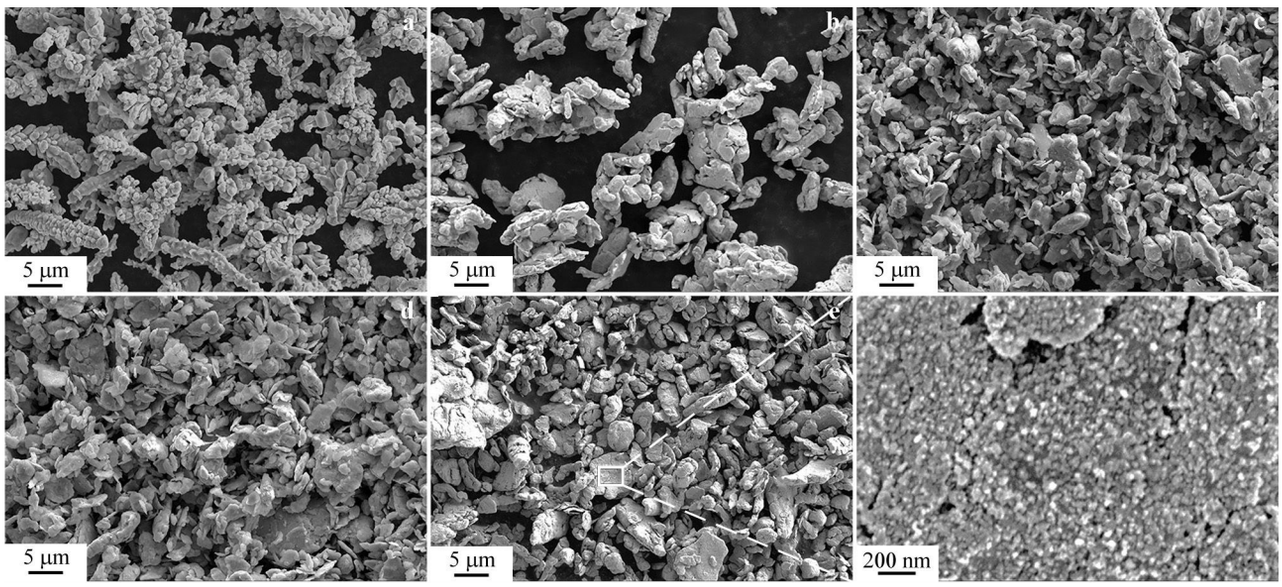

Fig.3 Morphologies of pure Cu powders and composite powders after thermal reduction: (a) original pure Cu powder; (b) Cu-36 h; (c) C-12 h; (d) C-24 h; (e–f) C-36 h

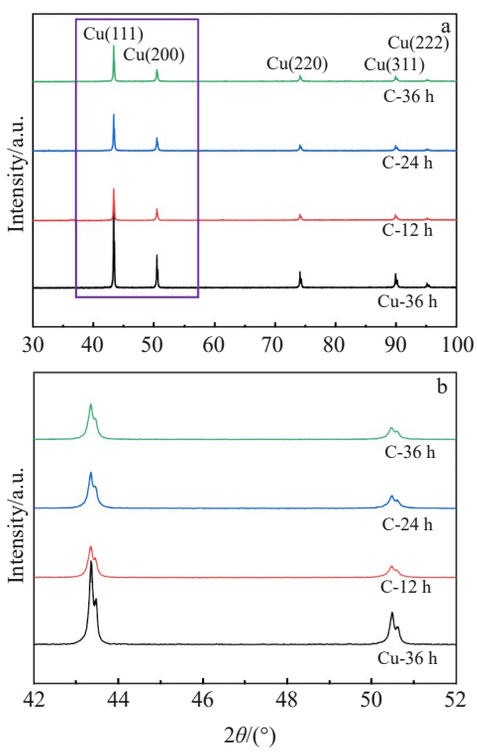

Fig.4 XRD patterns of pure Cu powders and composite powders after thermal reduction

Table 2 Relative density of bulk Cu-36 h and composites (%)

Material	Relative density
Cu-36 h	98.4
C-12 h	98.7
C-24 h	98.0
C-36 h	98.0

367±264 nm, respectively, indicating that high-volume-fraction ultrafine grains are successfully introduced into the composites, as shown in Fig. 6a$_2$ – 6d$_2$. The percentage of ultrafine grains in the composites is obviously larger than that in Cu-36 h, reaching 68.6% for C-36 h, as listed in Table 3. The high-volume-fraction ultrafine grains in Cu/Al_2O_3 composites are considered to arise primarily from the combined structure of Cu ultrafine powders covered with in-situ Al_2O_3 nanoparticles during low-temperature and high-pressure sintering.

The KAM distributions of Cu-36 h and composites are shown in Fig. 7. Relatively high microstrain and geometrically necessary dislocation (GND) density are mainly observed at the coarse grain region and grain boundary for Cu-36 h and composites. The detailed KAM values are listed in Table 4, indicating that the KAM values of C-24 h and C-36 h are slightly higher than those of Cu-36 h. Fig. 8 shows the XRD results of Cu-36 h and the composites. The FWHM of the Cu phase increases with prolonging the ball milling durations, and the second-phase nanoparticles are not detected due to the limited resolution. The microstrain ε and dislocation density ρ of metal materials can be evaluated by Eq. (1) and Eq. (2), respectively[26–27].

$$B\cos\theta = \frac{K\lambda}{d} + \varepsilon\sin\theta \quad (1)$$

$$\rho = \frac{2\sqrt{3}\,\varepsilon}{db} \quad (2)$$

where B is the true peak broadening, θ is the Bragg angle, λ is the wavelength (0.154 nm) of Cu Kα, K is about 0.9[27], d is the average grain size, and b is the Burgers vector (0.256 nm for Cu)[8]. The microstrain of Cu-36 h is slightly higher than that of the composites, and there is a high density of dislocations in both Cu-36 h and the composites, as shown in Fig. 8b. The average dislocation density of the composite

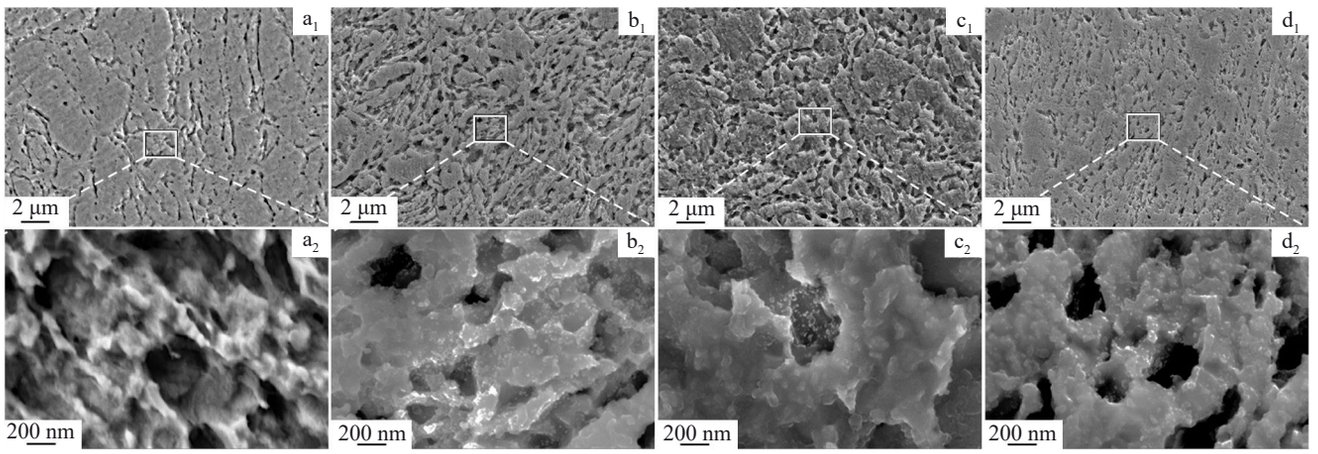

Fig.5 SEM images of deeply chemically etched Cu-36 h and composites: (a_1–a_2) Cu-36 h, (b_1–b_2) C-12 h, (c_1–c_2) C-24 h, and (d_1–d_2) C-36 h

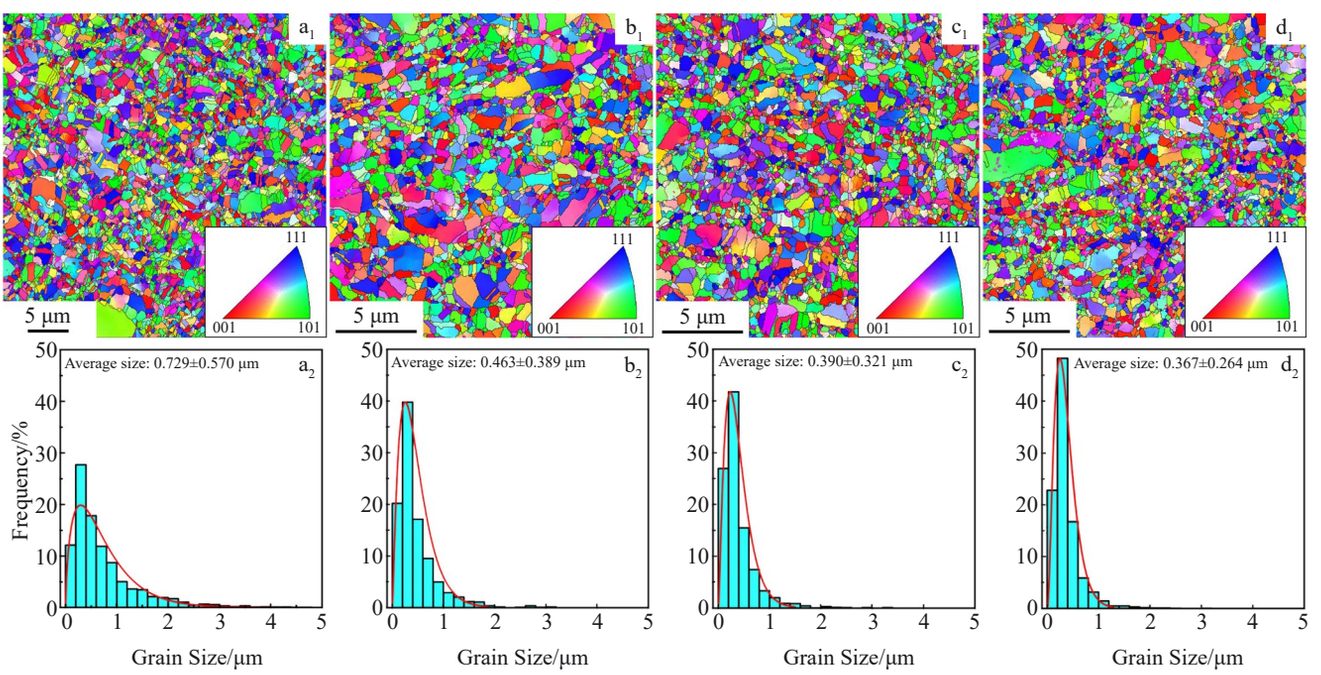

Fig.6 EBSD images (a_1–d_1) and grain size distributions (a_2–d_2) of Cu-36 h and composites: (a_1–a_2) Cu-36 h, (b_1–b_2) C-12 h, (c_1–c_2) C-24 h, and (d_1–d_2) C-36 h

Table 3 Percentage of ultrafine grains (grain size≤1 μm) in Cu-36 h and composites

Material	Percentage/%
Cu-36 h	20.2
C-12 h	45.3
C-24 h	55.4
C-36 h	68.6

increases with the ball milling time, and the average dislocation density of C-36 h is obviously higher than that of Cu-36 h.

The Cu grain microstructures and distributions of in-situ Al_2O_3 nanoparticles in bulk composites were investigated by TEM, as shown in Fig.9 and Fig.10. The Cu grain size varies from 100 nm to 400 nm, and a high density of dislocations originating in low-temperature and high-pressure sintering are observed in Fig. 9, which correspond to the KAM and XRD results. Fig. 10a – 10c show many second-phase nanoparticles in the composites, and C-12 h presents obvious agglomeration of second-phase nanoparticles. The EDS elemental analysis of the second-phase nanoparticles is shown in Fig. 10d. The results show that the second-phase nanoparticles primarily contain Al and O, which are derived from the in-situ Al_2O_3 nanoparticles. With prolonging the ball milling durations, the second-phase nanoparticles are distributed more homogeneously within the Cu grains, and the average sizes of the nanoparticles reach 15.3±15.0 and 11.7±7.5 nm for C-24 h and C-36 h, respectively, as shown in Fig. 10e – 10f. In addition, it is worth noting that the smaller in-situ Al_2O_3

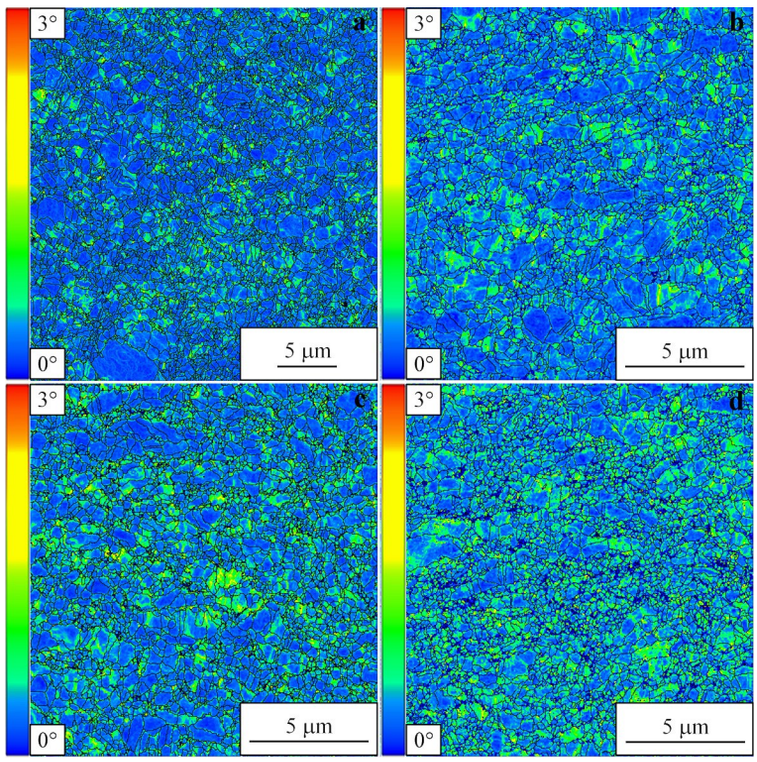

Fig.7 KAM distributions of Cu-36 h and composites: (a) Cu-36 h, (b) C-12 h, (c) C-24 h, and (d) C-36 h

Table 4 Average misorientation of Cu-36 h and composites

Material	KAM value/(°)
Cu-36 h	0.39
C-12 h	0.39
C-24 h	0.45
C-36 h	0.46

nanoparticles are mainly dispersed in the Cu grain interior, while some nanoparticles with a size larger than 30 nm are located at the grain boundaries. Subsequently, a detailed analysis of the phase structures of the in-situ Al_2O_3 nanoparticles and matrix is conducted by high-resolution TEM (HRTEM) observation, as shown in Fig. 11. The in-situ Al_2O_3 nanoparticles and Cu matrix are bonded at the atomic scale without defects or gaps, and the interface between them is smooth. To illustrate the orientation relationship, the fast Fourier transformation (FFT) and inverse fast Fourier transformation (IFFT) were carried out to investigate the interfacial microstructure between in-situ Al_2O_3 nanoparticles and Cu matrix, as shown in Fig. 11b–11d. The results show that the diffraction spots of the in-situ Al_2O_3 nanoparticles and Cu matrix are nearly overlapped, as shown in Fig. 11d. The (111) crystal plane of Cu and the (311) crystal plane of Al_2O_3 are approximately parallel to each other with interplanar spacings of 0.2095 and 0.2079 nm, respectively. The lattice mismatch (δ) between the (111) crystal plane of Cu and the (311) crystal plane of Al_2O_3 can be calculated by the following equation[28]:

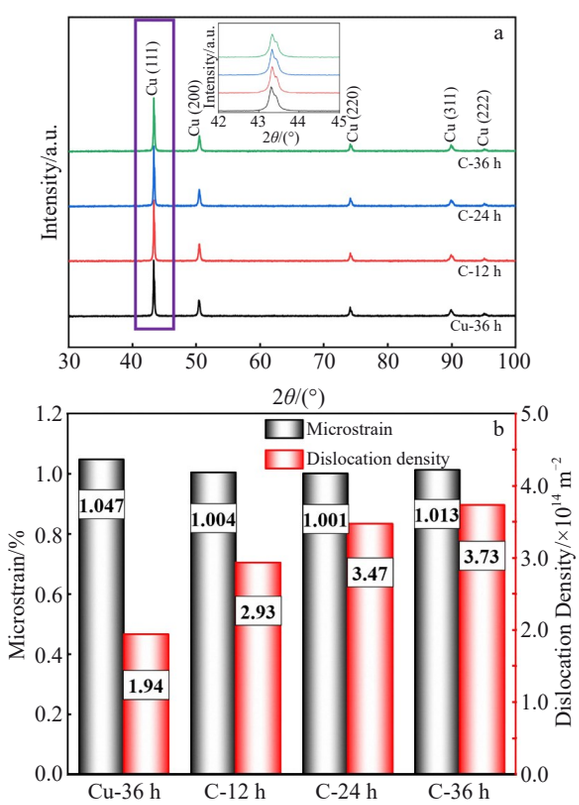

Fig.8 XRD patterns (a) and microstrain and dislocation density (b) of Cu-36 h and composites

$$\delta = \frac{|d_{Cu(111)} - d_{Al_2O_3(311)}|}{d_{Al_2O_3(311)}} \times 100\% = 0.8\% \ll 5\% \quad (3)$$

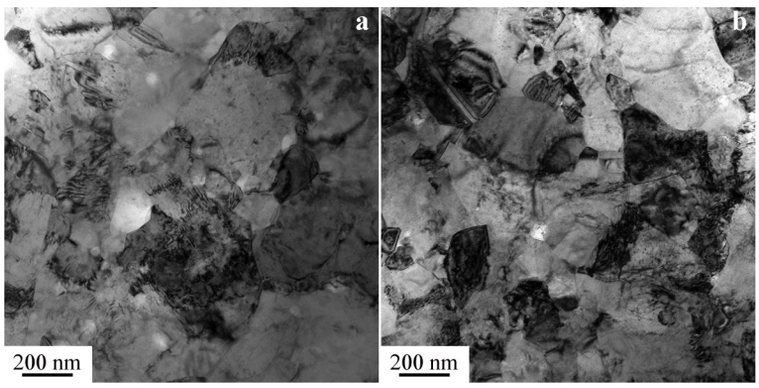

Fig.9 TEM images of composites C-24 h (a) and C-36 h (b)

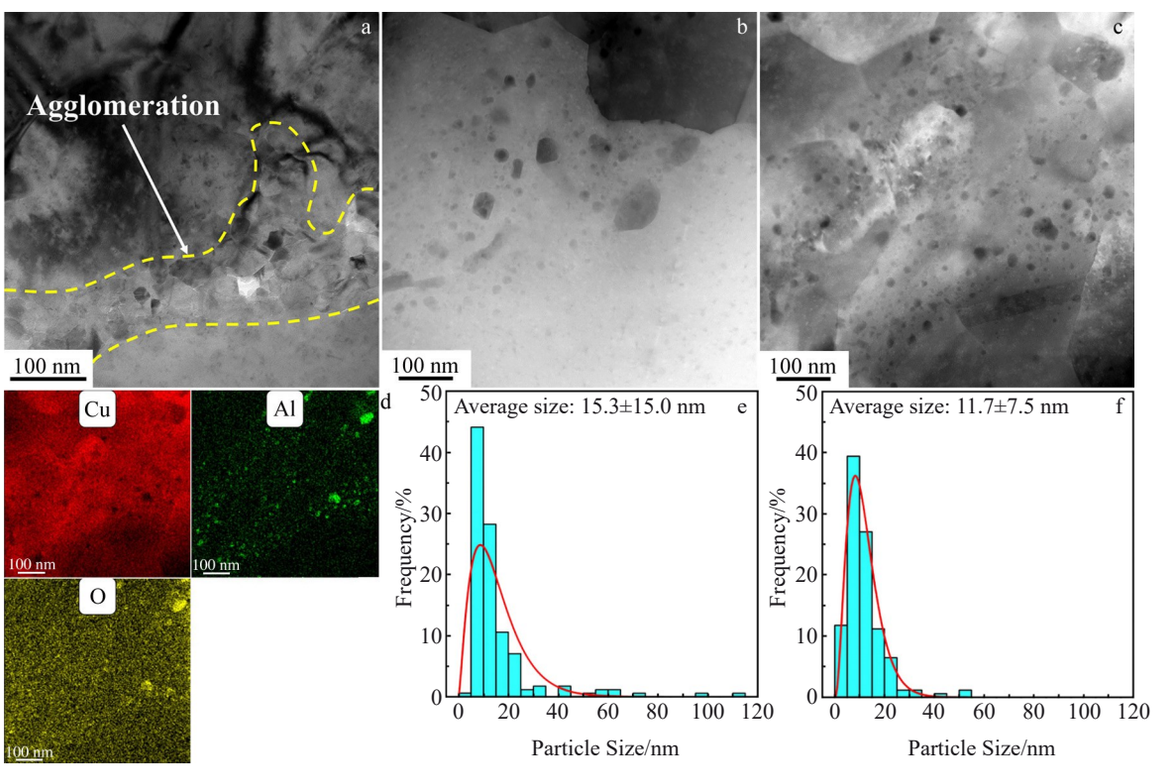

Fig.10 TEM image of C-12 h (a); HAADF images of C-24 h (b) and C-36 h (c); EDS elemental mappings corresponding to Fig. 10c (d); size distributions of in-situ Al_2O_3 nanoparticles in composites C-24 h (e) and C-36 h (f)

Obviously, the interface between the in-situ Al_2O_3 nanoparticles and the Cu matrix is confirmed to have a fully coherent relationship, which can reduce the interfacial energy and is conducive to improving the overall performance.

3.3 Mechanical and electrical properties

The typical engineering tensile stress-strain curves and electrical conductivities of Cu-36 h and composites are shown in Fig. 12, and the detailed parameters are listed in Table 5. In comparison with Cu-36 h, all composites display improved tensile strength and reduced electrical conductivity. With increasing the ball milling time, the yield strength (YS) and ultimate tensile strength (UTS) increase from 483±11 MPa to 555±6 MPa and from 563±4 MPa to 654±1 MPa for the composites, respectively, indicating that the addition of the in-situ Al_2O_3 nanoparticles can enhance the UTS by 45.3% and the YS by 50.8%. Meanwhile, the fracture elongation (EL) decreases slightly to 3.8%±0.6% and the electrical conductivity sustains 84.5%±0.1% IACS for C-36 h. Fig. 13 shows the SEM fracture surface morphologies of tensile Cu-36 h and composites. Many dimples are found in the Cu-36 h and composites, indicating the representative characteristics of plastic fracture. The quantity of nanoscale dimples in the composites is obviously higher than that in Cu-36 h due to the larger volume fractions of ultrafine grains, and plenty of in-situ Al_2O_3 nanoparticles are observed in the dimples of the composites, corresponding to the SEM results in Fig.5b_2–5d_2.

Fig. 14 presents the comprehensive comparison of mechanical and electrical properties between the present

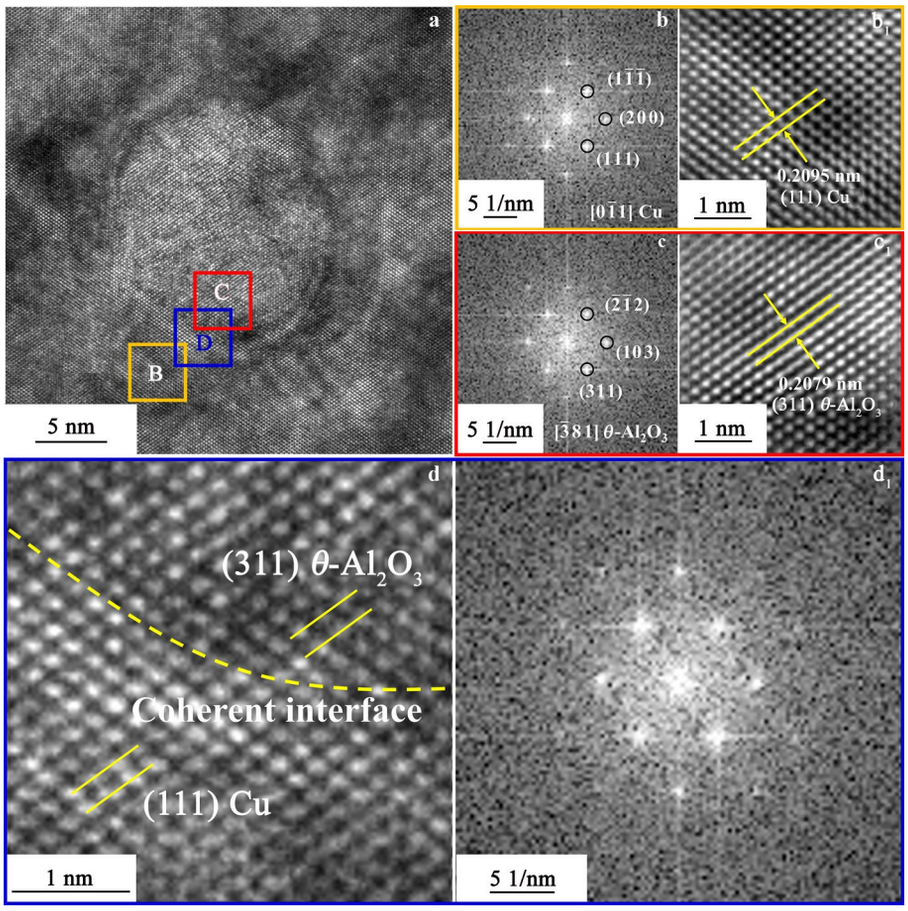

Fig.11 HRTEM image of interfacial structures of C-36 h (a); FFT (b–c) and IFFT (b_1–c_1) patterns of area B (b, b_1) and area C (c, c_1) marked in Fig.11a; enlarged image (d) and FFT pattern (d_1) of area D marked in Fig.11a

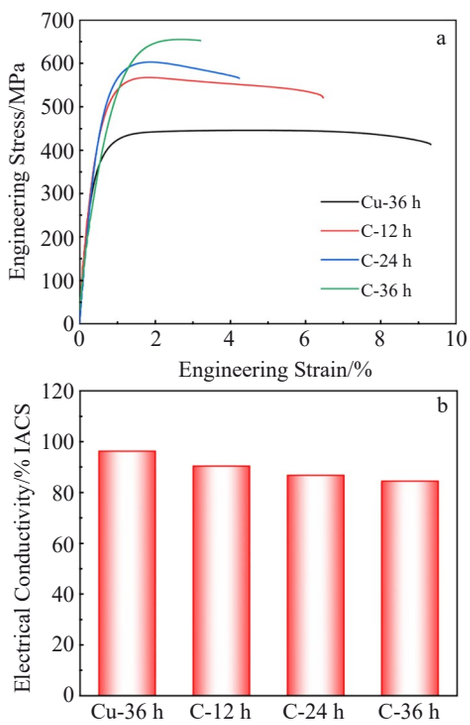

Fig.12 Engineering tensile stress-strain curves (a) and electrical conductivities (b) of Cu-36 h and composites

composites and published results. Fig. 14a shows that a comparably high tensile strength can be achieved even though the content of Al_2O_3 nanoparticles in the present study is obviously lower than that in other composites[8,29–36]. Meanwhile, Fig. 14b certifies that the composite in this study exhibits a superior balance of tensile strength and electrical conductivity than other reparted composites[4,8,29–34,37–38], confirming that the introduction of high-volume-fraction ultrafine grains can effectively enhance the strength without sacrificing the electrical conductivity remarkably.

3.4 Achievement of high-volume-fraction ultrafine grains

The above results show that Cu/Al_2O_3 composites with high-volume-fraction ultrafine grains can be fabricated by adopting ultrafine composite powder followed by low-temperature and high-pressure sintering. Apparently, an increased volume fraction and decreased grain size of ultrafine grains in Cu/Al_2O_3 composites are achieved by prolonging the ball milling durations (Fig.6). Increasing the ball milling time also favorably reduces the average size of in-situ Al_2O_3 nanoparticles and promotes the homogeneous distribution of those nanoparticles, as shown in Fig. 10. Additionally, the sintering temperature plays a key role in controlling the grain size. Zhang et al[25] reported that the Cu grain size was no more than 260 nm when the pure Cu nanopowder was

Table 5 Mechanical and electrical properties of Cu-36 h and composites

Material	UTS/MPa	$YS_{0.2\%}$/MPa	EL/%	Electrical conductivity/% IACS
Cu-36 h	450±5	368±3	10.5±1.2	96.3±0.1
C-12 h	563±4	483±11	5.4±1.1	90.5±0.2
C-24 h	610±7	545±35	3.7±0.5	86.8±0.3
C-36 h	654±1	555±6	3.8±0.6	84.5±0.1

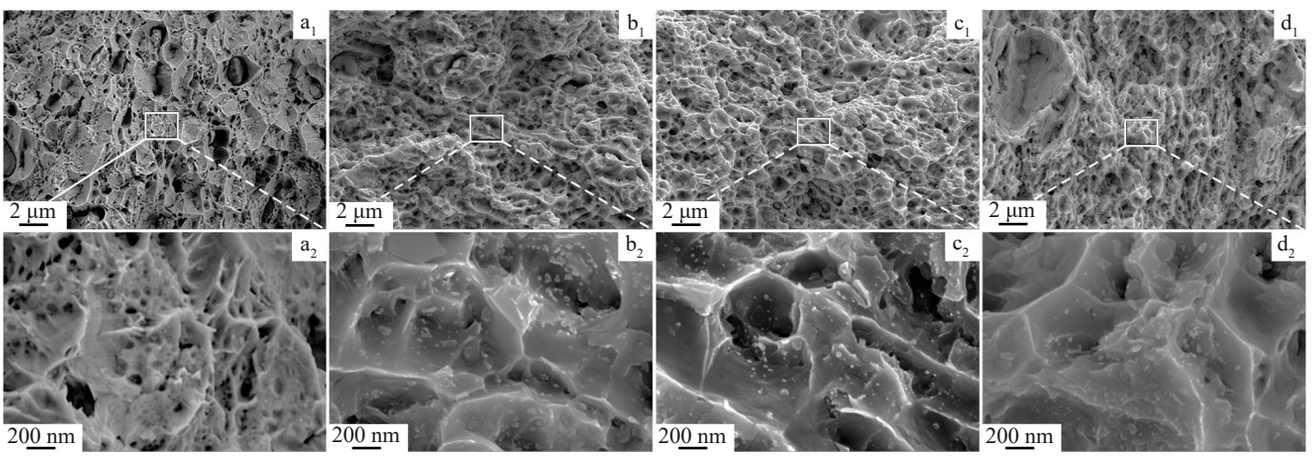

Fig.13 SEM fracture surface morphologies of Cu-36 h and composites after tensile tests: (a_1–a_2) Cu-36 h, (b_1–b_2) C-12 h, (c_1–c_2) C-24 h, and (d_1–d_2) C-36 h

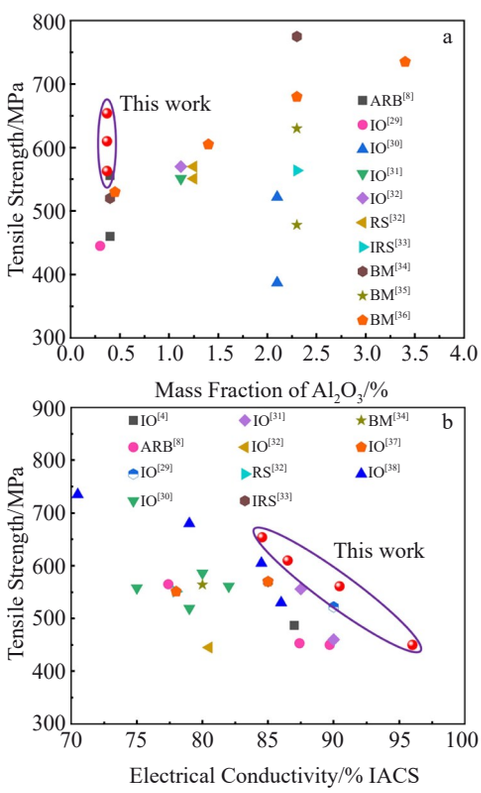

Fig.14 Property comparison of Cu/Al_2O_3 composites prepared by different methods: (a) tensile strength vs mass fraction of Al_2O_3, (b) tensile strength vs electrical conductivity (ARB: accumulative roll-bonding; IO: internal oxidation; RS: reaction synthesis; IRS: in-situ reactive synthesis; BM: ball milling)

consolidated at temperatures lower than 500 ℃, because the grain boundaries were difficult to migrate and grain growth could be restricted. Furthermore, the uniformly dispersed in-situ Al_2O_3 nanoparticles covering the surfaces of the Cu ultrafine powders can also effectively prevent grain growth. Thus, high-volume-fraction ultrafine grains are generated in the Cu/Al_2O_3 composites after low-temperature and high-pressure sintering. Interestingly, a superior balance of strength and electrical conductivity is achieved in the Cu/Al_2O_3 composites containing low-content reinforcement.

3.5 Strengthening mechanism of Cu/Al_2O_3 composites

The increase in YS of the Cu/Al_2O_3 composites is mainly attributed to the synergistic strengthening effect of grain refinement, dislocations, and in-situ Al_2O_3 nanoparticles, which can be evaluated by the following equation[39]:

$$\sigma_{cy} = \sigma_{my} + \Delta\sigma_{gb} + \Delta\sigma_{dis} + \Delta\sigma_{p} \quad (4)$$

where σ_{cy} and σ_{my} are YS of composites and Cu-36 h, respectively; $\Delta\sigma_{gb}$, $\Delta\sigma_{dis}$, and $\Delta\sigma_{p}$ represent the increments of YS by grain refinement, dislocations, and in-situ Al_2O_3 nanoparticles, respectively.

The EBSD results show that the average grain size of the composite is obviously smaller than that of Cu-36 h, and the strength increment contribution from grain refinement can be estimated by the following Hall-Petch relationship[40–41]:

$$\Delta\sigma_{gb} = K_H\left(d_c^{-0.5} - d_m^{-0.5}\right) \quad (5)$$

where K_H is the Hall-Petch coefficient (0.142 $MPa\cdot m^{0.5}$ for Cu)[8,33]; d_c and d_m are the average grain sizes of the composites and Cu-36 h, respectively. The detailed data of the evaluated $\Delta\sigma_{gb}$ of the composites are listed in Table 6. It can be seen that

Table 6 Calculated strength increment contribution in composites

Materials	$\Delta\sigma_{gb}$/ MPa	$\Delta\sigma_{dis}$/ MPa	$\Delta\sigma_{p}$/ MPa	Prediction summation/MPa	Experimental YS/MPa
Cu-36 h	-	-	-	-	368
C-12 h	49	21	45	-	483
C-24 h	61	31	78	538	545
C-36 h	68	35	94	565	555

$\Delta\sigma_{gb}$ increases with prolonging the ball milling time, and reaches 68 MPa for C-36 h, because the composite powders become finer after a longer ball milling durations. Therefore, the decreasing trend of grain size is maintained after low-temperature and high-pressure sintering.

According to the KAM and XRD results, there is a high density of dislocations in the Cu-36 h and composites, and the strength increment contribution from dislocation can be estimated by the following Bailey-Hirsch relationship[42–43]:

$$\Delta\sigma_{dis} = M\alpha Gb\left(\sqrt{\rho_c} - \sqrt{\rho_m}\right) \quad (6)$$

where M is the Taylor factor (3.06 for the fcc polycrystalline matrix); α is a constant (0.2 for fcc metals)[42]; ρ_c and ρ_m are the dislocation densities of composites and Cu-36 h, respectively; G is the shear modulus (42.1 GPa for Cu)[39]. As shown in Fig. 8b, the dislocation density increases with the ball milling time. Correspondingly, the calculated strength increment contribution from dislocations increases and reaches 21, 31, and 35 MPa for C-12 h, C-24 h and C-36 h, respectively.

For composites, the calculated $\Delta\sigma_{gb}$ and $\Delta\sigma_{dis}$ are much smaller than the total increment of YS. The remaining strength contribution mainly derives from the strengthening effect of in-situ Al_2O_3 nanoparticles by forming Orowan looping, which can be calculated by the following Orowan-Ashby equation[44]:

$$\Delta\sigma_{p} = \frac{0.13Gb}{\lambda_p}\ln\frac{d_p}{2b} \quad (7)$$

where d_p is the average particle diameter, and λ_p is the interparticle spacing. Assuming that the in-situ Al_2O_3 nanoparticles are uniformly distributed within the composite, the interparticle spacing can be approximately calculated by the following formula[45]:

$$\lambda_p = d_p\left(\frac{\pi}{6V_p}\right)^{\frac{1}{3}} \quad (8)$$

where V_p is the volume fraction of in-situ Al_2O_3 nanoparticles. The average size of the in-situ Al_2O_3 nanoparticles is determined by TEM observation, as shown in Fig. 10. The calculated strength increment contributions from in-situ Al_2O_3 nanoparticles are 78 and 94 MPa for C-24 h and C-36 h, respectively, while the theoretical calculation is unsuitable for C-12 h due to the obvious agglomeration of in-situ Al_2O_3 nanoparticles, as shown in Fig. 10a. Assuming that the total strength increment contribution in composites is originated from the synergistic strengthening effect of grain refinement, dislocations, and in-situ Al_2O_3 nanoparticles, the strength contribution from in-situ Al_2O_3 nanoparticles can be evaluated as 45 MPa for C-12 h.

Based on the above analysis, the strength increment contribution from grain refinement, dislocations, and in-situ Al_2O_3 nanoparticles is summarized with the YS of Cu-36 h, and the theoretical YS values are estimated as 538 and 565 MPa for C-24 h and C-36 h, respectively, which are in good accordance with the experimental values, as shown in Table 6. The strengthening effect of each factor increases with prolonging the ball milling time, and the increment contribution order of YS is $\Delta\sigma_p > \Delta\sigma_{gb} > \Delta\sigma_{dis}$ for all composites except C-12 h. These results demonstrate that the proposed strategy can introduce high-volume-fraction ultrafine grains accompanied by a high density of dislocations, thus significantly improving the mechanical properties of the materials.

3.6 Electrical conductivity

The electrical resistivity of composites can be estimated by the following Matthiessen's rule[46]:

$$\rho_{total} = \rho_{Cu} + \rho_{gb} + \rho_{d} + \rho_{p} \quad (9)$$

where ρ_{Cu} is the electrical resistivity of pure Cu; ρ_{gb}, ρ_{d}, and ρ_{p} represent the electrical resistivities caused by grain boundaries, dislocations, and in-situ Al_2O_3 nanoparticles, respectively. Usually, the electrical resistivity of composites increases with increasing the density of grain boundaries, dislocations, and in-situ Al_2O_3 nanoparticles. Tian et al[47] reported that the electron scattering induced by grain boundaries is not ignorable when the grain size is close to its electron mean free path. The average grain size of C-36 h is 367±264 nm, approximately ten times the electron mean free path (40 nm within the Cu grain)[48]. Hence, the electrical resistivity caused by grain boundaries will not obviously increase. Furthermore, the dislocation density of the composites is much less than $10^{15}/m^2$ (Fig. 8b); thus, the electrical resistivity caused by dislocations is smaller than 10^{-10} Ω·m, which can also be negligible[49]. The influence of second-phase nanoparticles on electrical resistivity can be illustrated by the following Schroeder equation[50]:

$$\rho_{p} = \rho_{Me}\left(\frac{3V_p}{2\left(1 - V_p\right)}\right) \quad (10)$$

$$\rho_{Me} = \rho_{Cu} + \rho_{gb} + \rho_{d} \quad (11)$$

Due to the relatively low content of Al_2O_3 nanoparticles (0.4wt%) in the present study, the electrical resistivity caused by Al_2O_3 nanoparticles is far smaller than the summation (ρ_{Me}) of electrical resistivities caused by pure Cu, grain boundaries, and dislocations[29]. Therefore, the obtained C-36 h maintains a high electrical conductivity of 84.5%±0.1% IACS when its tensile strength reaches a much higher value of 654±1 MPa.

4 Conclusions

1) High-volume-fraction ultrafine grains accompanied by a high density of dislocations can be introduced into Cu/Al_2O_3 composites via chemical and mechanical alloying followed by low-temperature and high-pressure sintering.

2) The average sizes of the Cu grains and in-situ Al_2O_3 nanoparticles reach 367±264 and 11.7±7.5 nm in the obtained

composite, respectively, and a coherent interface forms between the in-situ Al_2O_3 nanoparticles and the Cu matrix simultaneously.

3) The composite achieved an excellent balance of high strength and high electrical conductivity, and the increase in yield strength is mainly ascribed to the synergistic strengthening effect of ultrafine grains, dislocations, and in-situ Al_2O_3 nanoparticles.

4) This strategy can be easily applied to other reducible metals (such as Ni and Mo) and inorganic salts (such as $Y(NO_3)_3$ and $La(NO_3)_3$) for synthesizing high-performance metal matrix composites with high-volume-fraction ultrafine grains.

References

1 Qin Y Q, Tian Y, Peng Y Q *et al. Journal of Alloys and Compounds*[J], 2020, 848: 156475

2 Jing Y B, Gan C L, Miao Y P *et al. Rare Metal Materials and Engineering*[J], 2023, 52(7): 2364

3 Guo T B, Feng R, Li K Z *et al. Rare Metal Materials and Engineering*[J], 2023, 52(7): 2396

4 Lee J, Kim Y C, Lee S *et al. Metallurgical and Materials Transactions A*[J], 2004, 35: 493

5 Wang Q J, Fan R X, Liu D *et al. Rare Metal Materials and Engineering*[J], 2022, 51(2): 414

6 Lu L, Shen Y, Chen X *et al. Science*[J], 2004, 304(5669): 422

7 Schiøtz J, Jacobsen K W. *Science*[J], 2003, 301(5638): 1357

8 Chen F, Mei Q S, Li C L *et al. Materials Characterization*[J], 2021, 178: 111205

9 Zhang D. *Progress in Materials Science*[J], 2022, 123: 100853

10 Zhou D, Wang X, Zeng W *et al. Journal of Alloys and Compounds*[J], 2018, 753: 18

11 Zhang X, Jin S, Yang C *et al. Journal of Alloys and Compounds*[J], 2021, 862: 158687

12 Suryanarayana C, Al-Aqeeli N. *Progress in Materials Science*[J], 2013, 58(4): 383

13 Lee D W, Ha G H, Kim B K. *Scripta Materialia*[J], 2001, 44(8–9): 2137

14 Ke J, Xie Z, Liu R *et al. Materials*[J], 2022, 15(7): 2416

15 Dong Z, Ma Z, Yu L *et al. Nature Communications*[J], 2021, 12(1): 5052

16 Liu G, Zhang G J, Jiang F *et al. Nature Materials*[J], 2013, 12(4): 344

17 Dong Z, Ma Z, Liu Y. *Acta Materialia*[J], 2021, 220: 117309

18 Suryanarayana C. *Progress in Materials Science*[J], 2001, 46(1–2): 1

19 Suryanarayana C, Ivanov E, Boldyrev V V. *Materials Science and Engineering A*[J], 2001, 304: 151

20 Zhang D L. *Progress in Materials Science*[J], 2004, 49(3 – 4): 537

21 Zhou D, Wang X, Muránsky O *et al. Materials Science and Engineering A*[J], 2018, 730: 328

22 Li Z, Zhang Y, Zhang Z *et al. Nature Communications*[J], 2022, 13(1): 5581

23 Han L, Liu J, Tang H *et al. Materials Chemistry and Physics*[J], 2019, 221: 322

24 Ratzker B, Sokol M. *Materials & Design*[J], 2023, 233: 112238

25 Zhang Z H, Wang F C, Lee S K *et al. Materials Science and Engineering A*[J], 2009, 523(1–2): 134

26 Williamson G K, Hall W H. *Acta Metallurgica*[J], 1953, 1(1): 22

27 Ma K, Wen H, Hu T *et al. Acta Materialia*[J], 2014, 62: 141

28 Zhou Y, Yi G, Zhang P *et al. Journal of Nuclear Materials*[J], 2022, 560: 153484

29 Feng X, Zhang D, Feng B *et al. Journal of Materials Engineering and Performance*[J], 2022, 31(2): 1241

30 Ren F, Zhi A, Zhang D *et al. Journal of Alloys and Compounds*[J], 2015, 633: 323

31 Li C, Xie Y, Zhou D *et al. Materials Characterization*[J], 2019, 155: 109775

32 Zhang X H, Lin C G, Cui S *et al. Rare Metal Materials and Engineering*[J], 2016, 45(4): 893

33 Zhang X H, Li X X, Chen H *et al. Materials & Design*[J], 2016, 92: 58

34 Zhou D, Zeng W, Zhang D. *Journal of Alloys and Compounds*[J], 2016, 682: 590

35 Nachum S, Fleck N A, Ashby M F *et al. Materials Science and Engineering A*[J], 2010, 527(20): 5065

36 Zhou D S, Zhang D L, Kong C *et al. Materials Science and Engineering A*[J], 2013, 584: 67

37 Song K, Xing J, Dong Q *et al. Materials Science and Engineering A*[J], 2004, 380(1–2): 117

38 Tian B H, Xia C D, Jia S G. *Advanced Materials Research*[J], 2010, 148: 416

39 Long F, Guo X, Song K *et al. Composites Part B: Engineering*[J], 2022, 229: 109455

40 Hansen N. *Scripta Materialia*[J], 2004, 51(8): 801

41 Peng Y, Gao P, Zhang W *et al. Materials Characterization*[J], 2023, 205: 113281

42 Wen H, Topping T D, Isheim D *et al. Acta Materialia*[J], 2013, 61(8): 2769

43 Bailey J E, Hirsch P B. *Philosophical Magazine*[J], 1960, 5(53): 485

44 Zhang Z, Chen D L. *Scripta Materialia*[J], 2006, 54(7): 1321

45 Chen B, Shen J, Ye X *et al. Acta Materialia*[J], 2017, 140: 317

46 Mao Q, Wang L, Nie J *et al. Composites Part B: Engineering*[J], 2022, 231: 109567

47 Tian L, Anderson I, Riedemann T *et al. Acta Materialia*[J], 2014, 77: 151

48 Xiong L, Shuai J, Liu K *et al. Composites Part B: Engineering*[J], 2019, 160: 315

49 Liao W, Hu Y, Liu Q. *Materials Science and Engineering A*[J],

2022, 846: 143283 2007, 55(14): 4741

50 Phani P S, Vishnukanthan V, Sundararajan G. *Acta Materialia*[J],

引入高体积分数超细晶实现Cu/Al_2O_3复合材料优异的强度和导电性组合

张 军[1,2]，刘 溪[2,3]，李 毅[2,3]，常 国[2,4]，彭浩然[2,4]，张 霜[2,4]，黄 埼[1]，赵雪妮[1]，李 亮[2,4]，霍望图[2,4]

(1. 陕西科技大学 机电工程学院，陕西 西安 710021)

(2. 西北有色金属研究院 先进材料研究所，陕西 西安 710016)

(3. 西安理工大学 材料科学与工程学院，陕西 西安 710048)

(4. 西北有色金属研究院 金属多孔材料全国重点实验室，陕西 西安 710016)

摘 要：高强度Cu/Al_2O_3复合材料与其低强度相比时通常展现出明显恶化的导电性。基于一种化学和机械合金化策略，制备了低含量增强体超细复合粉末并构建超细铜粉负载原位自生Al_2O_3纳米颗粒组合结构。在相对较低的烧结温度（550 ℃）固结后，引入高体积分数超细晶到Cu/Al_2O_3复合材料中，产生大量平均尺寸为11.7±7.5 nm的原位自生Al_2O_3纳米颗粒，其均匀分布在铜晶粒内部。结果表明，复合材料表现出优异的高强度（654±1 MPa）与高导电（84.5±0.1% IACS）组合，这主要归因于超细晶、位错和原位自生Al_2O_3纳米颗粒的协同强化效果。这种以低含量增强体超细复合粉末为前驱体随后低温高压烧结的方法可应用于高性能氧化物弥散强化合金的大规模工业生产。

关键词：Cu/Al_2O_3复合材料；超细晶；原位自生Al_2O_3纳米颗粒；强化机制；导电性

作者简介：张 军，男，1995年生，硕士生，陕西科技大学机电工程学院，陕西 西安 710021，E-mail：1264218662@qq.com